https://doi.org/10.1016/j.ultras.2018.03.008

Analytical Insight into "Breathing" Crack-induced Acoustic Nonlinearity with An Application to Quantitative Evaluation of Contact Cracks

Kai WANG[a‡], Menglong LIU[a], Zhongqing SU[a,*], Shenfang YUAN[b], Zheng Fan[c]

[a] *Department of Mechanical Engineering*

The Hong Kong Polytechnic University, Kowloon, Hong Kong SAR

[b] *State Key Lab of Mechanics and Control of Mechanical Structures*

Nanjing University of Aeronautics and Astronautics, Nanjing 210016, P.R. China

[c] *The School of Mechanical and Aerospace Engineering*

Nanyang Technological University, Singapore 639798, Singapore.

Submitted to Ultrasonics

(Initial submission on 12 December 2017; Revised and re-submitted on 5 February 2018)

---

‡ PhD student

* To whom correspondence should be addressed. Tel.: +852-2766-7818, Fax: +852-2365-4703;

Email: Zhongqing.Su@polyu.edu.hk (Prof. Zhongqing SU, *Ph.D.*);

Abstract

To characterize fatigue cracks, in the undersized stage in particular, preferably in a quantitative and precise manner, a two-dimensional (2D) analytical model is developed for interpreting the modulation mechanism of a "breathing" crack on guided ultrasonic waves (GUWs). In conjunction with a modal decomposition method and a variational principle-based algorithm, the model is capable of analytically depicting the propagating and evanescent waves induced owing to the interaction of probing GUWs with a "breathing" crack, and further extracting linear and nonlinear wave features (*e.g.*, reflection, transmission, mode conversion and contact acoustic nonlinearity (CAN)). With the model, a quantitative correlation between CAN embodied in acquired GUWs and crack parameters (*e.g.*, location and severity) is obtained, whereby a set of damage indices is proposed via which the severity of the crack can be evaluated quantitatively. The evaluation, in principle, does not entail a benchmarking process against baseline signals. As validation, the results obtained from the analytical model are compared with those from finite element simulation, showing good consistency. This has demonstrated accuracy of the developed analytical model in interpreting contact crack-induced CAN, and spotlighted its application to quantitative evaluation of fatigue damage.

***Keywords*:** "breathing" crack; contact acoustic nonlinearity; guided ultrasonic waves; analytical model; crack evaluation

1. Introduction

Fatigue damage, pervasive in engineering structures, has posed tremendous jeopardy to structural integrity and durability. Without timely awareness and subsequent remedial actions, fatigue damage can potentially lead to tragic consequences, incurring immense monetary wastage and even loss of life. Amongst various modalities of fatigue damage, the contact fatigue cracks are prevailing but most insidious. This sort of fatigue damage is usually initiated by deteriorative changes in material microstructures due to local accumulation of dislocations, high stress concentration, plastic deformation around inhomogeneous inclusions or other inherent imperfection, when a structure is subject to cyclic rolling and/or sliding contact loads. Progressive crack propagation from a microscopic to macroscopic degree subsequently leads to permanent damage at an observable extent[1].

The longer an engineering structure in service the more contact fatigue cracks it may develop. The presence of contact fatigue cracks in pivotal structural components (*e.g.*, aircraft engine turbine, rolling bearings or junction components in power plants) can be extraordinarily detrimental. Exemplarily, a train owned by Norfolk Southern in Columbus, the United States, detailed on July 11, 2012[2], leading to an urgent evacuation of hundreds of residents and vast economic loss. Later investigation has revealed that the fracture of a rail section, initiated by numerous contact fatigue cracks caused by rolling train wheels after years of service of the rail section, was the culprit of this disastrous case.

To detect contact fatigue cracks at an embryo stage, qualitatively at least if not quantitatively, is an imminent task to warrant a reliable service of key engineering structures, and a rigorously defined and functionally deployed structural health monitoring (SHM) technique can accommodate such a need. Amongst existing SHM techniques [3-7] the guided ultrasonic wave (GUW)-based SHM[8-11] has proven its superb capability to strike a balance among resolution, detectability, practicality and cost, by taking advantage of appealing features of GUWs including long-range and quick probing, omnidirectional dissemination, high penetration, great sensitivity to damage of small dimensions, and cost-effective implementation.

The majority of existing GUW-based SHM approaches evaluate material deterioration or structural damage based on changes in linear signal features[12, 13] related with present damages, such as delay in time-of-flight (ToF)[14], wave reflection and transmission[15], energy dissipation[16] and mode conversion[17]. Nevertheless, as commented earlier, the damage in real-world engineering structures usually initiates from imperceptible contact fatigue cracks that become conspicuous quite late. These fatigue cracks (with its characteristic dimension much smaller than the wavelength of the probing GUW) may not engender remarkable changes in linear GUW features. Therefore, when dealing with contact fatigue cracks, the SHM approaches relying on the use of linear GUW features may be out of their depth.

Recognition of the inefficiency of linear GUW features towards evaluating contact fatigue cracks has motivated alternative attempts to explore nonlinear features extracted from GUW signals at frequencies other than the excitation frequency of the probing GUW[18-20]. The nonlinear GUW features are commonly typified by the second-[18, 21, 22]/sub-harmonics[19], mixed frequency responses[23] (*e.g.*, nonlinear wave modulation spectroscopy), and shift of resonance frequency (*e.g.*, nonlinear resonant ultrasound spectroscopy)[24] to name a few, as comprehensively surveyed elsewhere[25]. Nonlinear GUW features have been proven capable of rendering enhanced detectability, sensitivity and accuracy compared with their linear counterparts. As an extra merit, nonlinear GUW features, deployed in a frequency domain, can bypass possible spatial interference from the inspected structure, therefore possessing good immunity to wave reflections and mode conversion at structural boundaries.

Various sources of nonlinearity have been scrutinized[14, 26, 27], on which basis the nonlinear GUW features, generated when a probing GUW interacts with a contact fatigue crack, are interpreted. The commonly recognized nonlinear sources include the contact acoustic nonlinearity (CAN), bi-linear stiffness, hysteresis, Hertzian contact,, thermo-elastic coupling effect, *etc*., as reviewed by D. Broda *et al.*[28]. These sources of nonlinearity jointly contribute to the manifestation of nonlinearities in captured GUW signals. In particular, the CAN has been recognized as one of the major sources to introduce nonlinearity, and has been the core of intensive research. Numerically, Wan *et al.*[29] studied the interaction between fundamental symmetric Lamb waves and a buried micro-crack in a thin plate using a finite-element method (FEM), showing a monotonic increasing relationship between the CAN and the length of the micro-crack. Shen and Giurgiutiu[30] adopted FEM to simulate the interaction between Lamb waves and a surface-breathing crack in a plate, giving similar results. Analytically, Solodov *et al.*[31] has examined the interaction between a contact crack and probing waves. By assuming a step-change in the material stiffness at the crack location, the generation of high-order harmonics induced by the crack was calibrated. Richardson[32], from an analytical perspective, explored the high-order harmonic generation, by depicting the motion of two surfaces of a crack (an unbonded interface between two media) under the modulation of traversing waves. In both studies, the probing waves were modelled as longitudinal waves, and this has essentially limited the investigation into a one-dimensional (1D) scenario. On the other hand, a two-dimensional (2D) GUW behaves differently from a

1D longitudinal wave, and it embraces both propagating and evanescent waves, each of which features multiple modes co-existing simultaneously. Superposition of individual wave modes affects the crack when a GUW traverses the crack, under which the motion of crack surfaces, in a 2D manner, is not a uniform motion throughout the entire crack surfaces as hypothesized in a 1D case. These diatheses jointly lead to a mechanism of CAN generation that is substantially different from 1D scenarios, making the existing 1D models largely fail to construe the modulation of contact fatigue cracks on propagating GUWs accurately.

With this motivation, the present work is aimed at achieving an analytical insight into the modulation of a 2D contact fatigue crack with "breathing" behaviors on GUWs. An analytical model is developed, to quantitatively interpret the underlying mechanism of CAN generation induced by a contact fatigue crack. With the model, both the propagating and evanescent waves, along with the converted modes at crack surfaces, can be depicted explicitly. An analytical prediction of the CAN generation, subjected to the severity of the crack, is obtained, on which basis a quantitative correlation between CAN embodied in acquired GUW signals and crack parameters (*e.g.*, location and severity) is ascertained. With such a correlation, the severity of a contact fatigue crack can be evaluated quantitatively.

This paper is organized as follows: modulation of a 2D "breathing" crack on propagating GUWs is modeled analytically, and detailed in the second section. The model illuminates the generation of high-order harmonics induced by the crack and predicts the crack-induced wave fields. In this section, a quantitative correlation between the nonlinear features of GUWs and crack parameters is derived; a set of linear and nonlinear indices is defined, for evaluating the severity of a contact fatigue crack. In the third section, the developed analytical model is validated against finite element simulation. Concluding remarks are presented in the last section.

2. Modulation of "breathing" crack on probing GUWS – a nonlinear perspective

Consider a 2D plate-like waveguide, as illustrated schematically in Fig. 1, in which a contact crack exists along the waveguide thickness, A probing GUW is introduced into the waveguide with a transmitter (*e.g.*, a piezoelectric wafer) from the upper surface of the waveguide, left to the crack; and the probing GUW, guided by the waveguide, takes the modality of Lamb waves, to interact with the crack and accordingly produces transmitted and reflected waves that are acquired via wave receivers (or other non-contact means such as laser interferometry), respectively right and left to the crack. GUWs in the waveguide encompass multiple wave modes including symmetric and antisymmetric Lamb modes.

Limit the discussion to a lower thickness-frequency product – the highlighted region in the dispersion curves of GUWs in the waveguide shown in Fig. 2, where only the fundamental symmetric (S_0) and anti-symmetric (A_0) Lamb modes exist. For this region, the S_0 mode features a higher velocity than that of the A_0 mode, which can be beneficial to avoid the contamination from the waves reflected by structural boundaries, and therefore is selected to trigger the "breathing" behavior of the crack and introduce nonlinearity into GUWs. The interaction between the probing GUW and the contact crack embraces the following two steps in a "breathing" cycle of the crack:

(1) when the crack closes during wave compression, the propagating GUW is transmitted without inducing wave scattering; and
(2) when the crack opens during wave dilation – the case shown in Fig. 1 – the propagating GUW is partially decoupled, producing wave reflection and transmission in the waveguide.

These two steps jointly introduce the “breathing” behavior of the crack, and consequently incurs wave scattering and mode conversion (*e.g.*, conversion of the S_0 mode to the A_0 mode, or generation of the first-order symmetric mode (S_1) if the frequency is larger than the cut-off frequency of the S_1 mode), to distort the probing GUW. It is therefore that a “breathing” crack can be deemed as a second wave source in the waveguide to introduce a new wave field that modulates the original wave field – called “*crack-induced second source*” (CISS hereinafter) in this study.

It is the time-dependent traits of CISS – present when the crack opens and absent otherwise – lead to the generation of CAN. In the following, the amplitude of the CISS-induced CAN is to be ascertained analytically, via a modal decomposition method, Fourier transform analysis and a variational principle-based algorithm, based on which a set of linear and nonlinear indices can be defined for quantitative evaluation of the crack severity. Such a framework is recapitulated in Fig. 3, and as detailed as below.

2.1. High-order harmonics induced by “breathing” crack

Assume that the crack in Fig. 1 opens at a particular moment, t_{open}, when the stress at the crack interface turns from the compressional to tensile status in a cycle of interaction between the probing GUW and the crack. Upon crack opening, the crack interface behaves the same as it does when the probing GUW traverses a fully opened, notch-like crack of the same through-thickness depth, in which both the propagating and evanescent waves are generated. Although the evanescent waves transfer no energy and decay exponentially as waves propagating, the evanescent waves do influence the stress and displacement fields in the vicinity of the crack[33] (to be demonstrated in what follows).

Mathematically, the propagating and evanescent waves correspond to the roots of the dispersive equations of Lamb waves in a 2D waveguide, defined as

$$\frac{\tan(qh)}{\tan(ph)} = \frac{4k^2 qp\mu}{\left(\lambda k^2 + \lambda p^2 + 2\mu p^2\right)\left(k^2 - q^2\right)}. \tag{1}$$

In the above, $p^2 = \frac{\omega^2}{c_L^2} - k^2$ and $q = \frac{\omega^2}{c_T^2} - k^2$; ω is the angular frequency, h the half the thickness of the waveguide, and k the wavenumber; μ and λ are the shear modulus and Lamé constant, respectively; c_L and c_T denote velocities of the longitudinal and transverse/shear modes, respectively.

Using a Newton-Raphson method [34], the solutions to Eq. (1) can be obtained, which comprise a finite number of real roots (corresponding to propagating waves) and pure imaginary roots (associated with evanescent waves), along with an infinite number of complex roots (also relevant to evanescent waves), in Fig. 4. The root with a negative imaginary value is physically meaningless, and only those with positive imaginary values (corresponding to evanescent waves) and the ones with pure real values (propagating waves) can be acquired in experiment. The stress and displacement fields of all the propagating and evanescent waves form a complete set of bases[35]. Via appropriate superposition of the bases, the stress ($\tilde{\sigma}(x_3)$) and particulate displacement ($\boldsymbol{u}(x_3)$) fields across the entire thickness of the waveguide (x_3) can be depicted as

$$\begin{aligned} \tilde{\sigma}(x_3) &= \textstyle\sum_n a_n \tilde{\sigma}^n, \\ \boldsymbol{u}(x_3) &= \textstyle\sum_n a_n \boldsymbol{u}^n, \end{aligned} \tag{2a}$$

where

$$\tilde{\sigma}^n = \tilde{\sigma}^n(x_3)e^{i(\omega t - k^n x_1)},$$
$$\boldsymbol{u}^n = \boldsymbol{u}^n(x_3)e^{i(\omega t - k^n x_1)}. \tag{2b}$$

In the above, x_1 and x_3 represent directions of the probing GUW propagation and waveguide thickness, respectively (Fig. 1); t is the time, and *N* an index to distinguish the order of Lamb wave modes in the waveguide; $\tilde{\sigma}^n$ and $\boldsymbol{u}^n$ are the stress tensor and displacement vector for the n^{th}-order Lamb wave mode, respectively; a_n and k^n are the amplitude and wavenumber of the n^{th}-order Lamb wave mode, respectively.

When the crack opens, the crack surfaces are stress-free, while the stress and displacement fields remain continuous in the waveguide underneath the crack tip. In Fig. 1, the stress tensor (throughout the entire thickness including the cracked region and the part underneath the crack tip) can be represented in terms of three normal components (*viz.*, σ_{11}, σ_{33} and σ_{13}), and the displacement vector can be depicted with two orthotropic components (*i.e.*, u_1 and u_3). Using a modal decomposition[36], taking into account all the propagating and evanescent waves, and applying boundary conditions at the location of the crack, it has

$$\tilde{\sigma}^{Crack+}(x_3)\cdot\boldsymbol{x}_1 = \begin{cases}\sum_n a_n\sigma_{11}^n \\ \sum_n a_n\sigma_{13}^n\end{cases} = \begin{cases}0 \\ 0,\end{cases} \quad \text{(for the right-side crack surface)} \tag{3}$$

$$\tilde{\sigma}^{Crack-}(x_3)\cdot\boldsymbol{x}_1 = \begin{cases}a_{Inc}\sigma_{11}^{Inc} + \sum_n a_{-n}\sigma_{11}^{-n} \\ a_{Inc}\sigma_{13}^{Inc} + \sum_n a_{-n}\sigma_{13}^{-n}\end{cases} = \begin{cases}0 \\ 0,\end{cases} \quad \text{(for the left-side crack surface)}$$

(4)

$$\sum_n a_n\boldsymbol{u}^n = a_{Inc}\boldsymbol{u}^{Inc} + \sum_n a_{-n}\boldsymbol{u}^{-n}, \quad \text{(for the part underneath the crack)}$$

(5)

$$\begin{cases}\sum_n a_n\sigma_{11}^n \\ \sum_n a_n\sigma_{33}^n \\ \sum_n a_n\sigma_{13}^n\end{cases} = \begin{cases}a_{Inc}\sigma_{11}^{Inc}+\sum_n a_{-n}\sigma_{11}^{-n} \\ a_{Inc}\sigma_{33}^{Inc}+\sum_n a_{-n}\sigma_{33}^{-n} \\ a_{Inc}\sigma_{13}^{Inc}+\sum_n a_{-n}\sigma_{13}^{-n}.\end{cases} \quad \text{(for the part underneath the crack)} \tag{6}$$

Note that the index n is applicable to both the propagating and evanescent waves, and in particular $-n$ indicates those wave modes propagating opposite to the probing GUW. $\boldsymbol{x}_1$ is a direction vector. $\tilde{\sigma}^{Crack-}(x_3)$ and $\tilde{\sigma}^{Crack+}(x_3)$ signify stress tensors on the left- and right-side cross-sections of the waveguide at the location of crack (including both the cracked region and the part underneath the crack), respectively. The incident probing GUW is labelled with the superscript " Inc " in equations. The coefficient a_n, an unknown complex to be correlated with the amplitude of the incident GUW, is denoted by a_{Inc}.

To solve Eqs. (3)-(6) numerically, a singular value decomposition (SVD) method[37] is recalled. In SVD, the infinite evanescent modes in Eqs. (3)-(6) are truncated up to the first *N* modes. A total of 20 modes (*i.e.*, *N*=20), as demonstrated in this study, suffice to embody the majority of the energy carried by the GUW propagating in the waveguide and therefore guarantee the accuracy of solutions. The cross-section of the waveguide at the location of crack is numerically discretized, and the distance between any two adjacent, discretized points measures 1/25 of the waveguide thickness. To examine the accuracy of such a discretization, an energy balance-based criteria is applied, in accordance with the fact that the total energy carried by all the scattered wave modes, including transmitted and reflected modes, is supposed to approximate to the energy of the incident probing GUW. In this study, the energy difference between the scattered wave modes and the probing GUW, during SVD with the current discretization resolution, is less than 5%, validating the accuracy of the model in depicting the stress and displacement fields in the crack vicinity.

With Eqs. (3)-(6), the amplitude of each wave mode (a_n) – a function of a_{Inc} – can be obtained. It can be seen that the stress and displacement fields at the crack are indeed the superposition of the stress and displacement fields of the incident probing GUW and those of the crack-induced waves (*viz.*, by CISS), as

$$\begin{aligned}
&\boldsymbol{u}^{Crack-}\left(x_3,t\right)=a_{Inc}\boldsymbol{u}^{Inc}+\sum\nolimits_n a_{-n}\boldsymbol{u}^{-n}\\
&\boldsymbol{u}^{Crack+}\left(x_3,t\right)=\sum\nolimits_n a_n\boldsymbol{u}^{n}\\
&\tilde{\sigma}^{Crack-}\left(x_3,t\right)=a_{Inc}\tilde{\sigma}^{Inc}+\sum\nolimits_n a_{-n}\tilde{\sigma}^{-n}\\
&\tilde{\sigma}^{Crack+}\left(x_3,t\right)=\sum\nolimits_n a_n\tilde{\sigma}^{n},
\end{aligned} \tag{7}$$

where $\boldsymbol{u}^{Crack-}$ and $\boldsymbol{u}^{Crack+}$ are the displacement vectors of discretized points on the left- and right-side cross-sections at the location of the crack, respectively.

With explicit depiction of the stress and displacement fields at the crack in the above, the CISS during the crack opening can be defined as,

$$\begin{aligned}
&\boldsymbol{CISS}^{open+}=\left(\tilde{\sigma}^{Crack+}-a_{Inc}\tilde{\sigma}^{Inc}\right)\cdot\boldsymbol{x}_1,\\
&\boldsymbol{CISS}^{open-}=\left(\tilde{\sigma}^{Crack-}-a_{Inc}\tilde{\sigma}^{Inc}\right)\cdot\boldsymbol{x}_1,
\end{aligned} \tag{8}$$

where $\boldsymbol{CISS}^{open+}$ and $\boldsymbol{CISS}^{open-}$ denote the CISS (a force vector) on the right- and left-side cross-sections at the location of crack, respectively. $\boldsymbol{CISS}^{open+}$ and $\boldsymbol{CISS}^{open-}$ are of the identical amplitude yet opposite orientation. Considering the amplitude is of interest in the model, $\boldsymbol{CISS}^{open+}$ and $\boldsymbol{CISS}^{open-}$ are consolidated into $\boldsymbol{CISS}^{open}$ in what follows. With Eq. (7), the gap of two crack surfaces can be attained by calculating the difference between the in-plane (x_1) displacement of the right- ($u_1^{Crack+}\left(x_3,t\right)$) and left-side ($u_1^{Crack-}\left(x_3,t\right)$) crack surfaces. When such a distance retreats to zero, namely

$$u_1^{Crack+}\left(x_3,t\right)-u_1^{Crack-}\left(x_3,t\right)=0\,, \tag{9}$$

the crack closes, and this particular moment is denoted as t_{close}. To solve Eq. (9) makes t_{close} available. Up to this point, both t_{open} and t_{close} of a "breathing" cycle of the contact crack have been determined, upon taking the influence of CISS-induced wave fields on the incident probing GUW into account.

When the probing GUW is continuously emitted into the waveguide via tranmitter and cyclically interacts with the "breathing" crack, CISS periodically introduces wave fields in accordance with the above analysis. In the 2D scenario, the displacement of each discretized point on the crack surface is, under a general circumstance, different from the others at a moment, while, from Eq. (9), the closer to the crack tip the earlier the point on the crack surface closes in a "breathing" cycle. For convenience of discussion, the moment at which the two points, which are respectively located at the center of the left- and right-side crack surfaces (called *mid-point pair* in what follows), commence to be in contact is adopted as the moment that the entire crack, as a whole, begins to close.

With the developed analytical model, Figure 5 shows the displacement history of the mid-point pair when the probing GUW is continuously emitted into the waveguide, to observe that:

(1) the crack is about to open when the displacement of mid-point pair (both have the same displacement before crack opens) reaches the maximum along the propagation direction of the probing GUW, which corresponds to the moment when the stress field at the crack turns from a compressional into a tensile phase; and
(2) the crack intends to close when the gap between the mid-point pair retreats to zero.

Note that the CISS-induced wave fields distort the incident probing GUW, influencing the “breathing” behaviors of the crack, and under such an influence the t_{close} is determined. By way of illustration, Figure 5 also compares the displacement history of the mid-point pair with (using the developed model) and without (using existing 1D models) consideration of the influence of CISS-induced wave fields, when the crack is at two representative degrees of severity (50% and 75% of the waveguide thickness). Discrepancy can be seen between models. The discrepancy, though at a slight degree, imposes significant effect on the amplitude of the “breathing” crack-induced high-order harmonics in the spectrum which is to be extracted at double excitation frequency – that is because the magnitude of the crack-induced CISS in frequency domain is sensitive to t_{open} and t_{close}, and a slight difference in t_{close} (due to ignorance of CISS-induced wave fields) can result in remarkable difference in accordingly ascertained magnitude of CAN. It is noteworthy that in a 1D scenario, the t_{open} and t_{close} are linked with the pre-stress which is prerequisite to close the interface, while that is not the case in a 2D scenario because the waveguide remains continuous (via the part underneath the crack) when the probing waves are traversing.

Further, to reflect the above periodical “breathing” behaviors of the contact crack, an indicator function, $f(t)$, is introduced to modulate $\boldsymbol{CISS}^{open}$, as

$$\boldsymbol{CISS}^{bre} = \boldsymbol{CISS}^{open} \cdot \mathrm{e}^{i\omega_0 t} \cdot f(t), \tag{10a}$$

where

$$f(t) = \begin{cases} 1, & t_{open} < t < t_{close} \\ 0, & t_{close} < t < t_{open} + T. \end{cases} \tag{10b}$$

In Eq. (10a), $\boldsymbol{CISS}^{bre}$ is the modulated CISS featuring “breathing” traits. T is the duration of a cycle of the probing GUW. ω_0 is the angular excitation frequency. The spectrum of

$\boldsymbol{CISS}^{bre}$ can be obtained by convoluting incident wave period function $\mathrm{e}^{i\omega_0 t}$ with the indicator function $f\left(t\right)$, as

$$F(\omega) = F(\boldsymbol{CISS}^{bre}) = \boldsymbol{CISS}^{open} \cdot F(\mathrm{e}^{i\omega_0 t}) \otimes F(f\left(t\right)), \tag{11}$$

where F denotes the operation of Fourier transform. The notation $\otimes$ represents the convolution operation. With Eq. (11), the harmonics of various orders can be obtained from the spectrum, as shown in Fig. 6.

In the spectrum, $\boldsymbol{CISS}^{bre}$ features a series of CISS, each respectively existing at multiples of ω_0. In particular, at ω_0 and $2\omega_0$, $\boldsymbol{CISS}^{bre}$ is

$$\boldsymbol{CISS}^{bre-\omega_0} = A_{\omega_0} \cdot \boldsymbol{CISS}^{open} \cdot e^{i\omega_0 t}, \text{ (at } \omega_0\text{)}, \tag{12a}$$

$$\boldsymbol{CISS}^{bre-2\omega_0} = A_{2\omega_0} \cdot \boldsymbol{CISS}^{open} \cdot e^{i2\omega_0 t}. \text{ (at } 2\omega_0\text{)}, \tag{12b}$$

where A_{ω_0} and $A_{2\omega_0}$ signify amplitudes of the excitation (ω_0) and double excitation frequency ($2\omega_0$) components obtained from the spectrum. $\boldsymbol{CISS}^{bre-\omega_0}$ and $\boldsymbol{CISS}^{bre-2\omega_0}$ defined by Eq. (12) analytically interpret the generation of the reflected and transmitted wave fields at ω_0, and generation of the second harmonic at $2\omega_0$, respectively.

The model shown in Fig. 1 can be deemed as a jointed waveguide, comprising two semi-infinite parts that are jointed via the continuous part underneath the crack tip. For each semi-infinite part, an CISS functions as an independent excitation source applied on the free end, whose through-thickness distribution can be obtained using Eq. (8) and is plotted in Fig. 7. In a “breathing” cycle of the crack, the second harmonic produced by $\boldsymbol{CISS}^{bre-2\omega_0}$ embraces both the propagating and evanescent waves, superposition of whose stress fields on the free end yields to $\boldsymbol{CISS}^{bre-2\omega_0}$, as

$$\begin{cases} CISS_1^{bre-2\omega_0} \\ CISS_3^{bre-2\omega_0} \end{cases} = \begin{cases} \sum b_n^{2\omega_0}\sigma_{11}^{n-2\omega_0} \\ \sum b_n^{2\omega_0}\sigma_{13}^{n-2\omega_0}, \end{cases} \tag{13}$$

where $b_n^{2\omega_0}$ is the amplitude of the n^{th}-order Lamb wave mode at $2\omega_0$, to be ascertained in the next step (Section 2. 2); $CISS_1^{bre-2\omega_0}$ and $CISS_3^{bre-2\omega_0}$ represent two decompositions of $\boldsymbol{CISS}^{bre-2\omega_0}$ in the x_1 and x_3 directions, respectively. $\sigma_{11}^{n-2\omega_0}$ and $\sigma_{13}^{n-2\omega_0}$ are the two decompositions of the stress tensor of the n^{th}-order Lamb wave mode at $2\omega_0$. For convenience of discussion, the location of the crack, where the two semi-infinite parts are jointed, is set as the origin of the coordinate system, as highlighted in Fig. 7 (*viz*., $x_1 = 0$ at the original location of the crack before its interaction with the probing GUW).

Based on the above derivation, it can be seen that the generation of the second harmonic of the probing GUW can be attributed to $\boldsymbol{CISS}^{bre-2\omega_0}$, and the generated wave fields can fully be depicted analytically using Eq. (13).

2.2. Propagating waves induced by CISS

With Eq. (13), one can further delineate the reflection and transmission wave fields at ω_0 or $2\omega_0$, from which CISS-induced propagating waves can be isolated from other wave modes. To this end, the variational principle[38] is recalled in the model. With $\boldsymbol{CISS}^{bre-2\omega_0}$, the variational principle for the motion of the waveguide is given by

$$\int_V \mathrm{Re}\left(\sigma_{ij,j}^{2\omega_0} - \rho\ddot{u}_i^{2\omega_0}\right)\mathrm{Re}\left(\delta u_i^{2\omega_0}\right)dv + \int_S \mathrm{Re}\left(CISS_i^{bre-2\omega_0} - \eta_j\sigma_{ji}^{2\omega_0}\right)\mathrm{Re}\left(\delta u_i^{2\omega_0}\right)ds = 0,$$

$$\left(i = 1,\ 3,\ j = 1,\ 3\right) \tag{14a}$$

where ρ is the density. "Re" denotes the real part of a complex number. V and S stand for the volume and surface of the waveguide, respectively. i denotes a dummy index (i=1 or 3). $u_i^{2\omega_0}$ and $\sigma_{ji}^{2\omega_0}$ ($\sigma_{ji}^{2\omega_0}=\sum b_n^{2\omega_0}\sigma_{ji}^{n-2\omega_0}$) are the excited displacement and stress fields in the waveguide when subjected to $CISS_i^{bre-2\omega_0}$. $\delta u_i^{2\omega_0}$ signifies the variation of $u_i^{2\omega_0}$. $\ddot{u}_i^{2\omega_0}$ is the second-order derivative of $u_i^{2\omega_0}$ with respect to time. $\sigma_{ij,j}^{2\omega_0}$ is the partial derivative of $\sigma_{ji}^{2\omega_0}$ in the direction of x_j. Specifically, on the upper and lower surfaces of the waveguide, $\eta_j=1$ (when $j=3$) and $\eta_j=0$ (when $j=1$); at the free end of each semi-infinite part where the CISS is applied, $\eta_j=1$ (when $j=1$) and $\eta_j=0$ (when $j=3$). Given the fact that the stress ($\sigma_{ji}^{2\omega_0}$) and displacement ($u_i^{2\omega_0}$) fields induced by $\boldsymbol{CISS}^{bre-2\omega_0}$ in Eq. (14a) are the superposition of the wave modes propagating in an infinite waveguide as mentioned earlier (Section 2. 1), all the volume integrals in Eq. (14a) vanish because each term in the superposition satisfies the differential equations of equilibrium, and this leads to

$$\int_S \mathrm{Re}\left(CISS_i^{bre-2\omega_0}-\eta_j\sigma_{ji}^{2\omega_0}\right)\mathrm{Re}\left(\delta u_i^{2\omega_0}\right)ds=0\,,\ \left(i=1,\,3,\ j=1,\,3\right). \tag{14b}$$

According to the variational principle[38], namely

$$\delta u_i^{2\omega_0}=\delta\left(b_m^{2\omega_0}\right)\cdot u_i^{m-2\omega_0},\qquad \left(m=1,\cdots,N\right) \tag{15}$$

where $b_m^{2\omega_0}$ is the amplitude of the m^{th}-order Lamb wave mode, $u_i^{m-2\omega_0}$ signifies the particulate displacement of the m^{th}-order Lamb wave mode along the i^{th} direction at $2\omega_0$, the surface integral in Eq. (14b) gives rise to

$$\int_S \mathrm{Re}\left\{\left[CISS_i^{bre-2\omega_0}-\eta_j\sum_n b_n^{2\omega_0}\cdot\sigma_{ji}^{n-2\omega_0}e^{ik_nx_1}\right]e^{i2\omega_0t}\right\}\cdot\mathrm{Re}\left\{\left[\delta\left(b_m^{2\omega_0}\right)\cdot u_i^{m-2\omega_0}e^{ik_mx_1}\right]e^{i2\omega_0t}\right\}ds=0. \tag{16}$$

Further, integrating Eq. (16) with respect to t spanning a complete period of the Lamb waves at $2\omega_0$, and in the meantime obtaining the value at the free end (when $x_1=0$ in Fig. 7), one has

$$\mathrm{Re}\left\{\int_{-h}^{h}\left[\overline{CISS}_i^{bre-2\omega_0}-\eta_j\cdot\sum_n\left(\bar{b}_n^{2\omega_0}\cdot\bar{\sigma}_{ji}^{n-2\omega_0}\right)\right]\delta\left(b_m^{2\omega_0}\right)\cdot u_i^{m-2\omega_0}dx_3\right\}=0, \qquad (17)$$

where the bar over a variable denotes its complex conjugate. Using the dummy index defined earlier, it has

$\overline{CISS}_i^{bre-2\omega_0}\cdot u_i^{m-2\omega_0}=u_1^{m-2\omega_0}\overline{CISS}_1^{bre-2\omega_0}+u_3^{m-2\omega_0}\overline{CISS}_3^{bre-2\omega_0}$, and

$\eta_j\cdot\sum_n\left(\bar{b}_n^{2\omega_0}\cdot\bar{\sigma}_{ji}^{n-2\omega_0}\right)\cdot u_i^{m-2\omega_0}=\sum_n\left(u_1^{m-2\omega_0}\bar{\sigma}_{11}^{n-2\omega_0}+u_3^{m-2\omega_0}\bar{\sigma}_{13}^{n-2\omega_0}\right)\bar{b}_n^{2\omega_0}$, whereby Eq. (17) can be re-written as

$$\mathrm{Re}\left\{\int_{-h}^{h}\left[\begin{array}{l}\left(u_1^{m-2\omega_0}\overline{CISS}_1^{bre-2\omega_0}+u_3^{m-2\omega_0}\overline{CISS}_3^{bre-2\omega_0}\right)-\\ \sum_n\left(u_1^{m-2\omega_0}\bar{\sigma}_{11}^{n-2\omega_0}+u_3^{m-2\omega_0}\bar{\sigma}_{13}^{-2\omega_0}\right)\bar{b}_n^{2\omega_0}\end{array}\right]\delta\left(b_m^{2\omega_0}\right)dx_3\right\}=0. \qquad (18)$$

Considering that $\delta\left(b_m^{2\omega_0}\right)$ can be an arbitrary complex, Eq. (18) is tenable only when the following condition is met

$$\int_{-h}^{h}\left(u_1^{m-2\omega_0}\overline{CISS}_1^{bre-2\omega_0}+u_3^{m-2\omega_0}\overline{CISS}_3^{bre-2\omega_0}\right)dx_3=\int_{-h}^{h}\sum_n\left(u_1^{m-2\omega_0}\bar{\sigma}_{11}^{n-2\omega_0}+u_3^{m-2\omega_0}\bar{\sigma}_{13}^{n-2\omega_0}\right)\bar{b}_n^{2\omega_0}dx_3. \qquad (19)$$

For the same reason as stated earlier, the wave modes considered is limited to the first 20 modes (*i.e.*, *N*=20) which carry the majority of the wave energy in the waveguide. To further simplify Eq. (19), let

$$\int_{-h}^{h}\left(u_1^{m-2\omega_0}\bar{\sigma}_{11}^{n-2\omega_0}+u_3^{m-2\omega_0}\bar{\sigma}_{13}^{n-2\omega_0}\right)dx_3=\left[M_{mn}\right]_{N\times N}, \quad \left(m=1,\cdots,N;\, n=1,\cdots,N\right) \qquad (20a)$$

where $\left[M_{mn}\right]$ is a matrix with a dimension of $N\times N$, and define the inverse of $\left[M_{mn}\right]$ as

$$\left[M_{mn}\right]^{-1}=\left[R\right]. \qquad (20b)$$

Multiplying $\left[R\right]$ with both sides of Eq. (19) yields

$$\left[\bar{b}_n^{2\omega_0}\right]_{N\times1} = \left[R\right]\cdot\int_{-h}^{h}\left(u_1^{m-2\omega_0}\,\overline{CISS_1^{bre-2\omega_0}} + u_3^{m-2\omega_0}\,\overline{CISS_3^{bre-2\omega_0}}\right)dx_3. \tag{21}$$

Using Eq. (21) and then substituting the analytical depiction of $\boldsymbol{CISS}^{bre-2\omega_0}$ (ascertained via Eq. (12b)) into Eq. (21), one can get the conjugate of the amplitude of every single wave mode (either propagating or evanescent wave) at $2\omega_0$ (*i.e.*, $\bar{b}_n^{2\omega_0}$), excited by the $\boldsymbol{CISS}^{bre-2\omega_0}$.

It is noteworthy that $\left[M_{mn}\right]$ in Eq. (20a), in terms of its physical interpretation, represents the average rate at which the work is done by the stress of m^{th}-order Lamb wave mode when this wave mode acts through the particulate displacement of the n^{th}-order Lamb wave mode – a coupling correlation between two wave modes propagating in the waveguide.

Along the same line of analysis, the reflected and transmitted wave fields at ω_0, which is attributed to the CISS induced by the crack at the excitation frequency (*i.e.*, $\boldsymbol{CISS}^{bre-\omega_0}$), can also be obtained.

Although both the propagating and evanescent waves are generated by the contact crack, the evanescent waves exist only in the vicinity of the crack and decay exponentially as wave propagating [33]. Thus, only the propagating waves (*e.g.*, S_0 mode), to be captured with a far-field receiver in experiment, are exploited in what follows. Bearing this in mind, the amplitudes of the propagating S_0 mode (in far field) at ω_0 induced by the $\boldsymbol{CISS}^{bre-\omega_0}$ and at $2\omega_0$ induced by $\boldsymbol{CISS}^{bre-2\omega_0}$ are denoted by $b_1^{\omega_0}$ and $b_1^{2\omega_0}$ (*viz.*, for S_0 mode, *n*=1), respectively. Thus, the displacement fields ($U_1^{\omega_0}$, $U_3^{\omega_0}$, $U_1^{2\omega_0}$ and $U_3^{2\omega_0}$) of the propagating crack-induced S_0 mode can be ascertained, as

$$U_1^{\omega_0} = b_1^{\omega_0} u_1^1\left(x_3\right), \quad U_3^{\omega_0} = b_1^{\omega_0} u_3^1\left(x_3\right), \tag{22a}$$

$$U_1^{2\omega_0} = b_1^{2\omega_0} u_1^{1-2\omega_0}\left(x_3\right), \quad U_3^{2\omega_0} = b_1^{2\omega_0} u_3^{1-2\omega_0}\left(x_3\right), \tag{22b}$$

where $U_1^{\omega_0}$ ($U_3^{\omega_0}$)and $U_1^{2\omega_0}$ ($U_3^{2\omega_0}$) are the in-plane (out of plane) displacement fields of the propagating S_0 mode at ω_0 and $2\omega_0$, respectively. $u_1^1\left(x_3\right)$ ($u_3^1\left(x_3\right)$) and $u_1^{1-2\omega_0}\left(x_3\right)$ ($u_3^{1-2\omega_0}\left(x_3\right)$) are the mode shape functions of the in-plane (out-of-plane) displacement fields of the propagating S_0 mode at ω_0 and $2\omega_0$, respectively.

Note that the magnitudes of CISS-generated second harmonics, as defined by Eq. (22b), in the reflected and transmitted waves are identical, because the magnitudes of the two $\boldsymbol{CISS}^{bre-2\omega_0}$ in both semi-infinite parts are the same. This implies that, in principle, during the evaluation of a contact crack using the crack-induced second harmonic, a “pulse-echo” configuration (for capturing reflected waves) and a “pitch-catch” configuration (for capturing transmitted waves) are equally feasible, with comparable sensitivity and accuracy. In a “pulse-echo” configuration, the reflected wave fields can be illustrated with Eq. (22a), while in a “pitch-catch” configuration, the influence of the incident probing GUW on the transmitted wave fields must be taken into account – that is to say the displacement fields of the propagating S_0 mode are the superposition of the incident probing GUW and the transmitted waves. Considering the probing GUW in this study takes the modality of S_0 mode (*viz.*, $u_i^{Inc} = u_i^1$), the said superposition is

$$U_1^{\omega_0} = a_{Inc} u_1^1\left(x_3\right) - b_1^{\omega_0} u_1^1\left(x_3\right), \quad U_3^{\omega_0} = a_{Inc} u_3^1\left(x_3\right) - b_1^{\omega_0} u_3^1\left(x_3\right). \tag{23}$$

2.3. Damage index for evaluating crack severity

Based on Eqs. (22) and (23), a set of dimensionless damage indices, making use of the nonlinear (extracted at $2\omega_0$) and linear (at ω_0) GUW features, is proposed, aimed at quantitatively evaluating the severity of a contact crack, defined as

$$NI = U_1^{2\omega_0} \Big/ \left(a_{Inc} u_1^1 (x_3)\right) = \left(b_1^{2\omega_0} u_1^{1-2\omega_0} (x_3)\right) \Big/ \left(a_{Inc} u_1^1 (x_3)\right), \tag{24a}$$

$$LI^R = b_1^{\omega_0} \Big/ a_{Inc}, \quad LI^T = \left(a_{Inc} - b_1^{\omega_0}\right) \Big/ a_{Inc}, \tag{24b}$$

where NI indicates a nonlinear index – a ratio of (i) the amplitude of the propagating S_0 mode at $2\omega_0$, induced by $\boldsymbol{CISS}^{bre-2\omega_0}$, to (ii) the amplitude of the probing GUW (S_0 mode). Linear-wise, for the purpose of comparison, two linear indices are defined: LI^R is the ratio of the amplitude of the crack-induced, reflected S_0 mode to the amplitude of the probing GUW (S_0 mode), and LI^T the ratio of the amplitude of the crack-induced, transmitted S_0 mode to the amplitude of the probing GUW (S_0 mode). In particular, for the case shown in Fig. 1, where the wave receiver is placed on the upper surface of the waveguide, NI can be evaluated at the upper surface when $x_3 = h$, as

$$NI = U_1^{2\omega_0} \Big/ a_{Inc} u_1^1 (x_3) = b_1^{2\omega_0} u_1^{1-2\omega_0} (h) \Big/ a_{Inc} u_1^1 (h). \tag{25}$$

With Eqs. (24) and (25), the nonlinear and linear indices can be obtained using the amplitude captured with a receiver, to evaluate the severity of a contact crack.

3. Validation using finite element-based simulation

To validate the developed analytical model, finite element (FE)-based simulation was performed. ABAQUS®/CAE was employed for modeling and ABAQUS®/EXPLICIT for simulation. An aluminum medium, 8 mm in thickness, 1000 mm in length and infinite in width – a 2D waveguide – was considered and modeled using both the FE and the analytical model. The material properties of the medium are listed in Table 1. The contact crack in the waveguide was modeled as a seam with different length – an edge with overlapping nodes that can be either in contact or apart under the modulation of the probing GUW. To model the contact interaction between the two crack surfaces, a surface-surface contact-pair definition, which prohibits the penetration of nodes into opposite surface was adopted to model the "breathing" behaviors of the contact crack. To ensure accuracy of simulation, at least ten FE nodes were allocated per wavelength of the GUW at $2\omega_0$. The simulations were carried out for cracks with different depth.

Hanning-window modulated 5-cycle sinusoidal tone bursts with a central frequency of 100 kHz were excited, by applying forces at a pair of FE nodes whose locations were symmetric about the middle plane of the waveguide, as illustrated schematically in Fig. 8. Two nodes on the top surface of the waveguide, respectively left and right to the crack, as shown in Fig. 8, were selected as wave receivers to capture GUW, on which the nodal displacements were acquired along x_1 (corresponding to the S_0 mode). Allowing for the dispersive and multimodal properties of GUWs, the thickness-frequency product of the probing GUW was selected to be 800 kHz·mm, as highlighted in Fig. 2, at which only S_0 and A_0 Lamb modes co-exist – two propagating wave modes which are barely dispersive at this frequency.

With the developed FE model, a representative cycle of the crack opening (in tensile phase of probing GUW) and closing (in compressional phase) is shown in Fig. 9, to observe that the tensile stress causes the crack to open and consequently the GUW traversing is interrupted (crack surfaces are stress-free), while the compressional stress drives the crack to close and GUW traverses the crack continuously without introducing conspicuous additional wave fields. Both jointly introduce nonlinearities to GUW signals captured by the receivers. For illustration, the time-series nodal displacement, captured by the receiver left to the crack – the reflected GUW from the crack, is displayed in Fig. 10. Applied with a short-time Fourier Transform (STFT) analysis, the signal spectrum is plotted in Fig. 11 (for two representative degrees of crack severity). From the spectrum, individual wave modes can be isolated by making a reference to the analytical dispersive curves, in Fig. 12(a). In the meantime, the amplitude of each wave mode at ω_0 and $2\omega_0$ are determined from the spectrum, exhibited in Fig. 12(b) (after normalized to the amplitude of the incident probing GUW).

With the known amplitude of each wave mode, the linear and nonlinear damage indices were calculated using Eqs. (24) and (25). A variety of degrees of crack depth, from 12.5% up to 98.75% of the waveguide thickness, was explored, in order to calibrate the relation between the crack depth and the linear/nonlinear GUW features induced by the contact crack. Such a correlation is shown in Fig. 13 (linear indices in Fig. 13(a), and nonlinear index in Fig. 13(b)). Good agreement can be observed between FE and analytical results, indicating the validity and accuracy of the developed analytical model.

At the embryo stage of a contact crack, for two linear indices, LI^R is noted to be trivial, while LI^T remains unchanged. This observation has corroborated an earlier statement in Section 1 that the linear features of GUWs are barely discernable for fatigue damage in an undersized stage, and this sort of signal features can become remarkable only when the severity of the damage crack reaches a certain extent – (30%) as observed in Fig. 13(a). For the nonlinear index, it can be seen from Fig. 13(b) that the severer a crack, the greater *NI* it will be, and the increasing rate of the nonlinear index tends to decrease when the crack depth reaches a certain degree (*i.e.*, 60% of the waveguide thickness). Similar trends were reported by Shen and Giurgiutiu[30], and Wan *et al.*[29], respectively, both concluding that the amplitude of CAN increased monotonically to a peak value and then tended to reach a plateau or decrease slightly. Inversely, the magnitude of the extracted CAN can be used to estimate the parameters of the crack. The monotonous correlation between the *NI* and crack depth indicates that the defined NI is capable of quantifying the severity of a contact crack. Compared with the material nonlinearity-induced second harmonic whose magnitude is usually three orders lower than that of the incident probing GUW, the CAN induced by a contact crack is prominent. It is also noteworthy that, from the analytical modeling, the position of the crack along the waveguide thickness is not a factor to affect the evaluation precision, and therefore the proposed detection framework is applicable to both surface and buried cracks.

Moreover, in conjunction with the use of the time-of-flight of the second harmonic, the location of the contact crack can be pinpointed using appropriate methods, such as the probability-based diagnostic imaging method[39]. In addition, in contrast to the methods based on the use of linear GUW features, the detection of the contact fatigue crack using CAN is immune to the adversity caused by the reflections and mode conversion at the boundaries. It is also noteworthy that upon the interaction of the contact crack with probing GUW, accompanying the generation of reflection and transmission, mode conversion is also to be induced, *e.g.*, A_0 can be generated when the symmetric waves traversing the crack, due to the antisymmetric geometry of the crack, as evident in Fig. 12. This has offered an alternative to define other types of damage indices in conjunction with the use of these converted wave modes.

4. Concluding remarks

Aimed at characterizing fatigue cracks in a quantitative manner, a dedicated analytical model is developed to interpret the modulation mechanism of a 2D "breathing" crack on probing GUWs. In conjunction with a modal decomposition method and a variational principle-based algorithm, the model is capable of scrutinizing the "breathing" behavior of the crack when the probing GUW traversing, and analytically depicting the "breathing" behavior-induced propagating and evanescent waves, from which linear and nonlinear signal characteristics (*e.g.*, CAN) can be extracted. With the model, a quantitative correlation between CAN embodied in acquired GUW signals and the crack parameters (*e.g.*, location and severity) is obtained, whereby a set of damage indices is proposed, able to quantitatively evaluate the severity of a contact crack. The evaluation, in principle, does not entail a benchmarking process. FE results well corroborate the analytical model. Further study will be focused on experimental validation and also the inclusion of internal stress, crack gaps, slanted incidence and crack roughness in the analytical model.

Acknowledgments

This work was supported by a Key Project of the National Natural Science Foundation of China [grant number 51635008] and the Hong Kong Research Grants Council via General Research Fund [grant number 15214414 and number 15201416].

References

[1] G. Fajdiga and M. Sraml, Fatigue crack initiation and propagation under cyclic contact loading, Engineering fracture mechanics, 76 (2009), 1320-1335.

[2] F. Zakar and E. Mueller, Investigation of a Columbus, Ohio train derailment caused by fractured rail, Case Studies in Engineering Failure Analysis, 7 (2016), 41-49.

[3] T. Ghosh, T. Kundu, and P. Karpur, Efficient use of Lamb modes for detecting defects in large plates, Ultrasonics, 36 (1998), 791-801.

[4] T. Hayashi, W.-J. Song, and J. L. Rose, Guided wave dispersion curves for a bar with an arbitrary cross-section, a rod and rail example, Ultrasonics, 41 (2003), 175-183.

[5] L. Yu and V. Giurgiutiu, In situ 2-D piezoelectric wafer active sensors arrays for guided wave damage detection, Ultrasonics, 48 (2008), 117-134.

[6] M. J. Lowe, D. N. Alleyne, and P. Cawley, Defect detection in pipes using guided waves, Ultrasonics, 36 (1998), 147-154.

[7] S. Chaki and G. Bourse, Guided ultrasonic waves for non-destructive monitoring of the stress levels in prestressed steel strands, Ultrasonics, 49 (2009), 162-171.

[8] Z. Su and L. Ye, *Identification of damage using Lamb waves: from fundamentals to applications* vol. 48: Springer Science & Business Media, 2009.

[9] D. N. Alleyne and P. Cawley, The interaction of Lamb waves with defects, IEEE transactions on ultrasonics, ferroelectrics, and frequency control, 39 (1992), 381-397.

[10] Y. Lu, L. Ye, Z. Su, and C. Yang, Quantitative assessment of through-thickness crack size based on Lamb wave scattering in aluminium plates, Ndt & E International, 41 (2008),

59-68.

[11]C. Eisenhardt, L. J. Jacobs, and J. Qu, Experimental Lamb wave spectra of cracked plates, REVIEW OF PROGRESS IN QUANTITATIVE NONDESTRUCTIVE EVALUATION: Volume 19 (2000), 343-350.

[12]Z. Su, L. Ye, and Y. Lu, Guided Lamb waves for identification of damage in composite structures: A review, Journal of sound and vibration, 295 (2006), 753-780.

[13]C. Zhou, Z. Su, and L. Cheng, Quantitative evaluation of orientation-specific damage using elastic waves and probability-based diagnostic imaging, Mechanical Systems and Signal Processing, 25 (2011), 2135-2156.

[14]A. Klepka, W. Staszewski, R. Jenal, M. Szwedo, J. Iwaniec, and T. Uhl, Nonlinear acoustics for fatigue crack detection–experimental investigations of vibro-acoustic wave modulations, Structural Health Monitoring, 11 (2012), 197-211.

[15]D. C. Betz, G. Thursby, B. Culshaw, and W. J. Staszewski, Identification of structural damage using multifunctional Bragg grating sensors: I. Theory and implementation, Smart materials and structures, 15 (2006), 1305.

[16]Z. Wu, X. P. Qing, and F.-K. Chang, Damage detection for composite laminate plates with a distributed hybrid PZT/FBG sensor network, Journal of Intelligent Material Systems and Structures,(2009),

[17]H. Sohn, D. Dutta, and Y.-K. An, Temperature independent damage detection in plates using redundant signal measurements, Journal of Nondestructive Evaluation, 30 (2011), 106.

[18]C. Zhou, M. Hong, Z. Su, Q. Wang, and L. Cheng, Evaluation of fatigue cracks using

nonlinearities of acousto-ultrasonic waves acquired by an active sensor network, Smart materials and structures, 22 (2012), 015018.

[19]C. Bermes, J.-Y. Kim, J. Qu, and L. J. Jacobs, Nonlinear Lamb waves for the detection of material nonlinearity, Mechanical Systems and Signal Processing, 22 (4// 2008), 638-646.

[20]J. Pei and M. Deng, Assessment of fatigue damage in solid plates using ultrasonic lamb wave spectra, 2008 IEEE Ultrasonics Symposium (2008), 1869-1872.

[21]D. Dutta, H. Sohn, K. A. Harries, and P. Rizzo, A nonlinear acoustic technique for crack detection in metallic structures, Structural Health Monitoring, 8 (2009), 251-262.

[22]T. Meurer, J. Qu, and L. Jacobs, Wave propagation in nonlinear and hysteretic media—a numerical study, International Journal of Solids and Structures, 39 (2002), 5585-5614.

[23]F. Aymerich and W. Staszewski, Experimental study of impact-damage detection in composite laminates using a cross-modulation vibro-acoustic technique, Structural Health Monitoring, 9 (2010), 541-553.

[24]M. Muller, A. Sutin, R. Guyer, M. Talmant, P. Laugier, and P. A. Johnson, Nonlinear resonant ultrasound spectroscopy (NRUS) applied to damage assessment in bone, The Journal of the Acoustical Society of America, 118 (2005), 3946-3952.

[25]K.-Y. Jhang, Nonlinear ultrasonic techniques for nondestructive assessment of micro damage in material: a review, International journal of precision engineering and manufacturing, 10 (2009), 123-135.

[26]V. Zaitsev, V. Gusev, and B. Castagnede, Thermoelastic mechanism for logarithmic slow dynamics and memory in elastic wave interactions with individual cracks, Physical review

letters, 90 (2003), 075501.

[27]I. Y. Solodov, N. Krohn, and G. Busse, CAN: an example of nonclassical acoustic nonlinearity in solids, Ultrasonics, 40 (2002), 621-625.

[28]D. Broda, W. Staszewski, A. Martowicz, T. Uhl, and V. Silberschmidt, Modelling of nonlinear crack–wave interactions for damage detection based on ultrasound—a review, Journal of Sound and Vibration, 333 (2014), 1097-1118.

[29]X. Wan, Q. Zhang, G. Xu, and P. W. Tse, Numerical simulation of nonlinear lamb waves used in a thin plate for detecting buried micro-cracks, Sensors, 14 (2014), 8528-8546.

[30]Y. Shen and V. Giurgiutiu, Predictive simulation of nonlinear ultrasonics, Proc. SPIE (2012), 83482E.

[31]I. Y. Solodov, Ultrasonics of non-linear contacts: propagation, reflection and NDE-applications, Ultrasonics, 36 (1998), 383-390.

[32]J. M. Richardson, Harmonic generation at an unbonded interface—I. Planar interface between semi-infinite elastic media, International Journal of Engineering Science, 17 (1979), 73-85.

[33]X. Yan and F.-G. Yuan, Conversion of evanescent Lamb waves into propagating waves via a narrow aperture edge, The Journal of the Acoustical Society of America, 137 (2015), 3523-3533.

[34]S. A. Teukolsky, B. P. Flannery, W. Press, and W. Vetterling, Numerical recipes in C, SMR, 693 (1992), 1.

[35]P. Kirrmann, On the completeness of Lamb modes, Journal of elasticity, 37 (1994), 39-

69.

[36]M. Castaings, E. Le Clezio, and B. Hosten, Modal decomposition method for modeling the interaction of Lamb waves with cracks, The Journal of the Acoustical Society of America, 112 (2002), 2567-2582.

[37]M. E. Wall, A. Rechtsteiner, and L. M. Rocha, "Singular value decomposition and principal component analysis," in *A practical approach to microarray data analysis*, ed: Springer, 2003, pp. 91-109.

[38]P. J. Torvik, Reflection of Wave Trains in Semi‐Infinite Plates, The Journal of the Acoustical Society of America, 41 (1967), 346-353.

[39]M. Hong, Z. Su, Y. Lu, H. Sohn, and X. Qing, Locating fatigue damage using temporal signal features of nonlinear Lamb waves, Mechanical Systems and Signal Processing, 60 (2015), 182-197.

Tables

Table 1 Material and physical properties of the aluminum used in FE validation

Density [kg/m^3]	Elastic modulus [GPa]	Poisson's ratio	C_L [m/s]	C_T [m/s]
2660	71.8	0.33	6324	3185

Figure Captions

Fig. 1 Schematic of a 2D infinite waveguide bearing a "breathing" crack when the crack is open

Fig. 2 Dispersion curve of Lamb waves in an aluminium waveguide

Fig. 3 Flowchart of the proposed framework to quantitatively analyse CAN induced by a "breathing" crack

Fig. 4 Roots to dispersive equation in a complex wavenumber domain

Fig. 5 Displacement history of a mid-point pair when the crack depth is (a) 50%; and (b) 75% of the waveguide thickness (with and without consideration of the influence of CISS-induced wave fields)

Fig. 6 (a) Indicator function based on Eq. (10); and (b) Spectrum of signal in (a)

Fig. 7 (a) Cross-thickness distribution of CISS; (b) two semi-infinite parts of the waveguide with CISS applied on the free end of each part

Fig. 8 The FE model for validation

Fig. 9 Snapshots of calculated stress fields when probing GUW traversing a "breathing" crack: (a) tensile stress causes crack to open and GUW traversing is interrupted; (b) compressional stress makes crack to close and GUW traverses continuously

Fig. 10 Nodal displacement history: black solid—in-plane; red dash—out-of-plane

Fig. 11 Spectra of the signal shown in Fig. 10 obtained using STFT when the crack depth is (a) 50%; and (b) 75% of the waveguide thickness

Fig. 12 (a) Spectra of the acquired reflection wave fields compared with the analytical dispersion curves; (b) comparison between the amplitude of incident GUW and the amplitude of the crack-induced waves at ω_0 and $2\omega_0$

Fig. 13 Defined linear/nonlinear indices *vs*. ratio of crack depth to the waveguide thickness: (a) linear indices; (b) nonlinear index

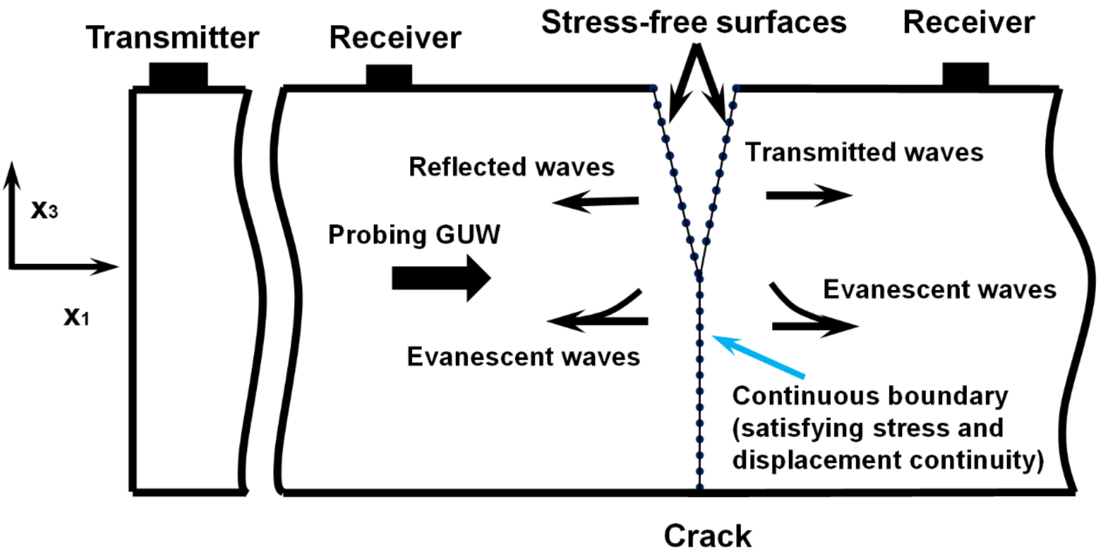
Transmitter
Receiver
Stress-free surfaces
Receiver
Reflected waves
Transmitted waves
x3
Probing GUW
x1
Evanescent waves
Evanescent waves
Continuous boundary
(satisfying stress and
displacement continuity)
Crack

Fig.1.

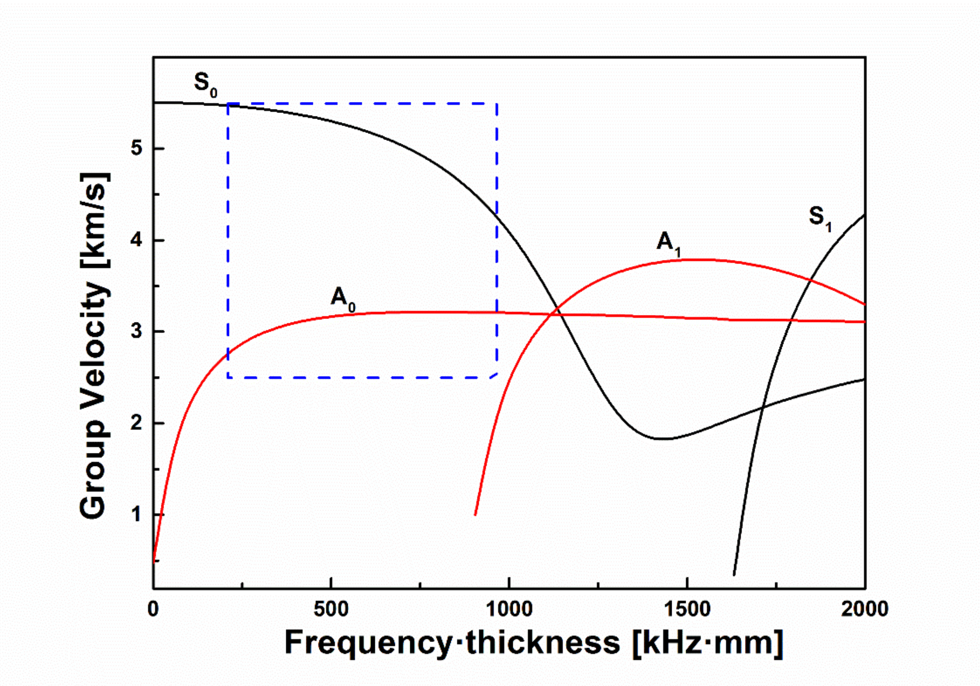
S0
S1
A0
A1
Group Velocity [km/s]
Frequency·thickness [kHz·mm]
0
500
1000
1500
2000
1
2
3
4
5

Fig. 2.

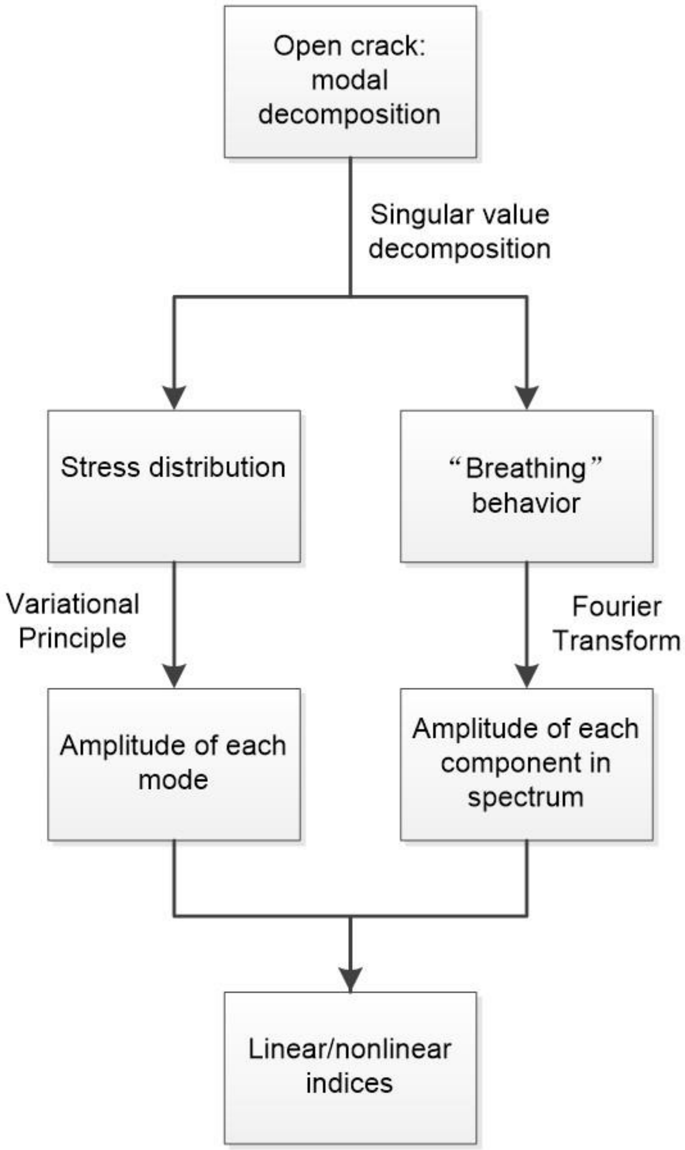
Open crack: modal decomposition
Singular value decomposition
Stress distribution
"Breathing" behavior
Variational Principle
Fourier Transform
Amplitude of each mode
Amplitude of each component in spectrum
Linear/nonlinear indices

Fig. 3.

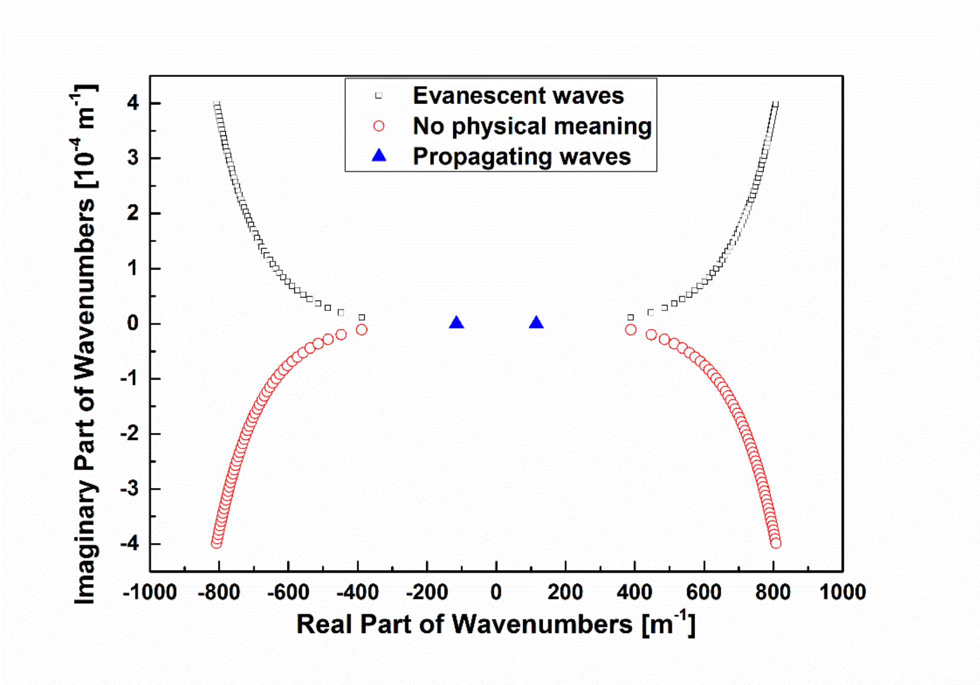
Evanescent waves
No physical meaning
Propagating waves
Imaginary Part of Wavenumbers [10^-4 m^-1]
Real Part of Wavenumbers [m^-1]
-1000
-800
-600
-400
-200
0
200
400
600
800
1000
4
3
2
1
0
-1
-2
-3
-4

Fig. 4.

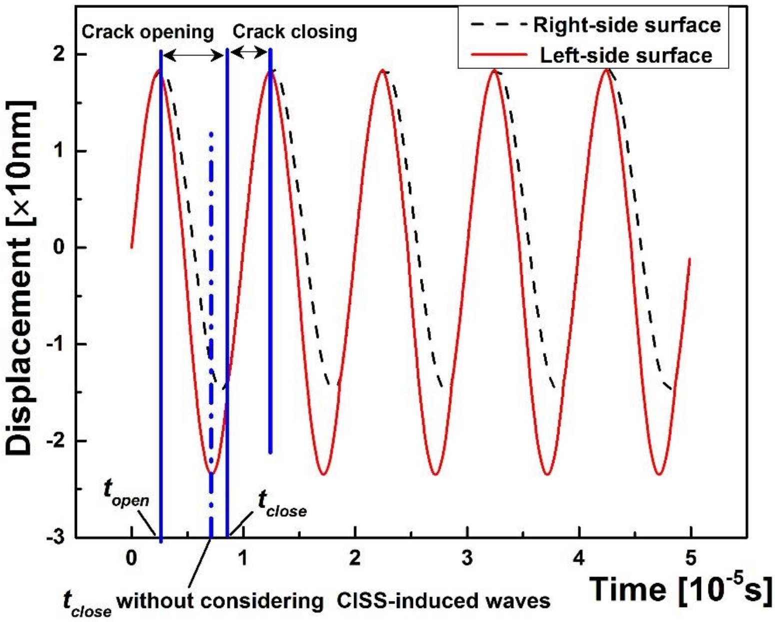
Crack opening
Crack closing
Right-side surface
Left-side surface
Displacement [×10nm]
2
1
0
-1
-2
-3
t_{open}
t_{close}
0
1
2
3
4
5
Time [10^{-5}s]
t_{close} without considering CISS-induced waves

Fig. 5(a)

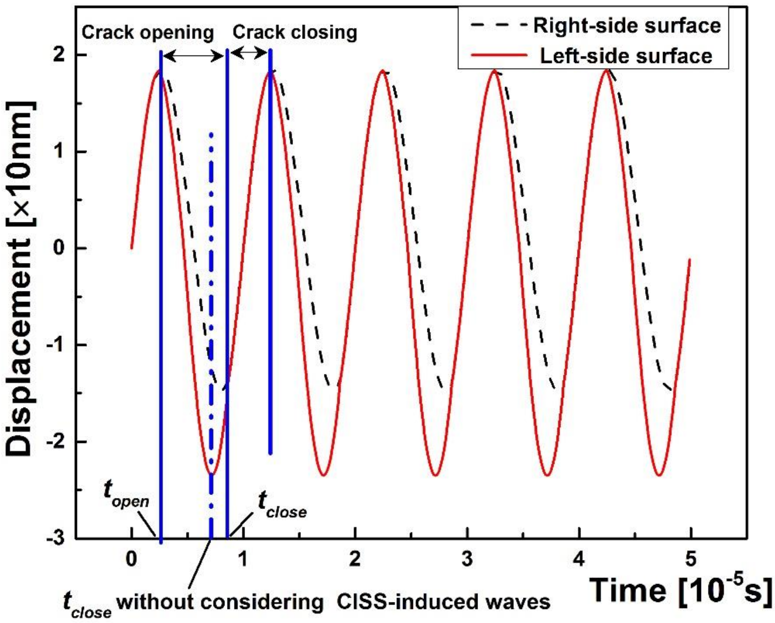
Crack opening
Crack closing
Right-side surface
Left-side surface
Displacement [×10nm]
2
1
0
-1
-2
-3
t_{open}
t_{close}
0
1
2
3
4
5
Time [10^{-5}s]
t_{close} without considering CISS-induced waves

Fig. 5(b)

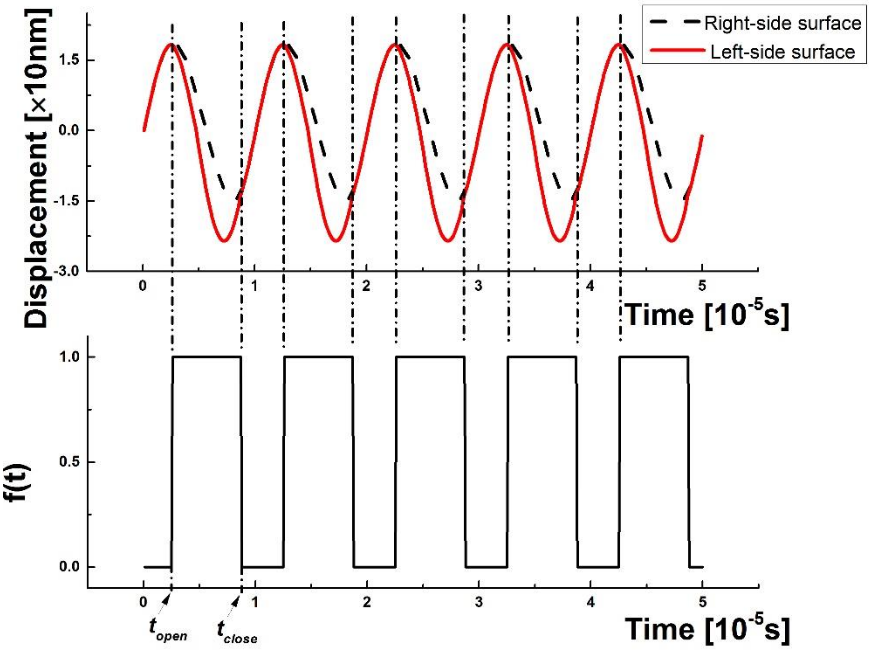

Right-side surface
Left-side surface
Displacement [×10nm]
Time [10^{-5}s]
f(t)
t_{open}
t_{close}

Fig. 6 (a)

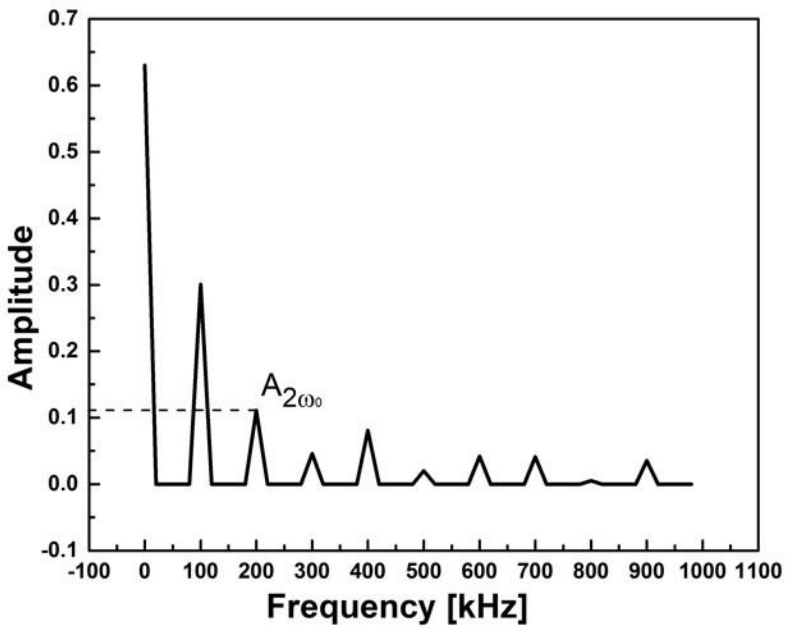

Amplitude
$A_{2\omega_0}$
Frequency [kHz]

Fig. 6(b)

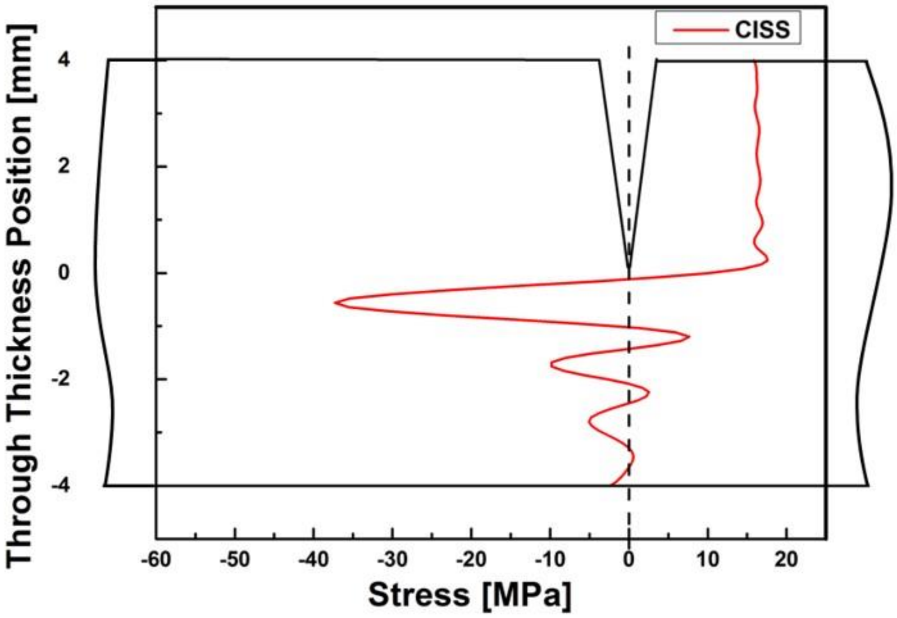
CISS
Through Thickness Position [mm]
4
2
0
-2
-4
-60
-50
-40
-30
-20
-10
0
10
20
Stress [MPa]

Fig. 7(a)

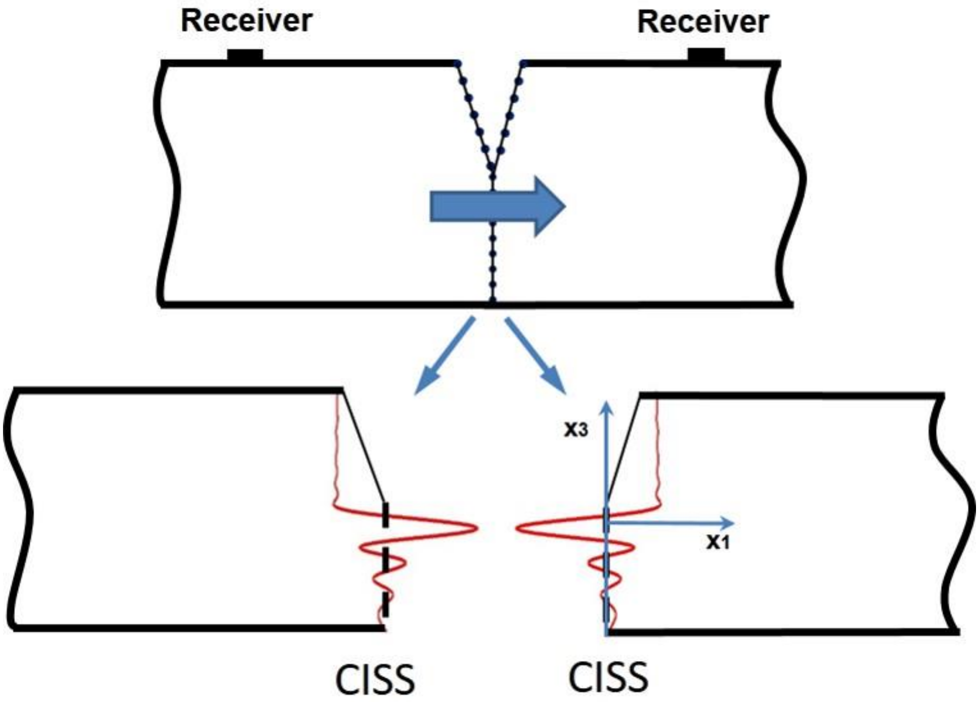
Receiver
Receiver
X3
X1
CISS
CISS

Fig. 7(b)

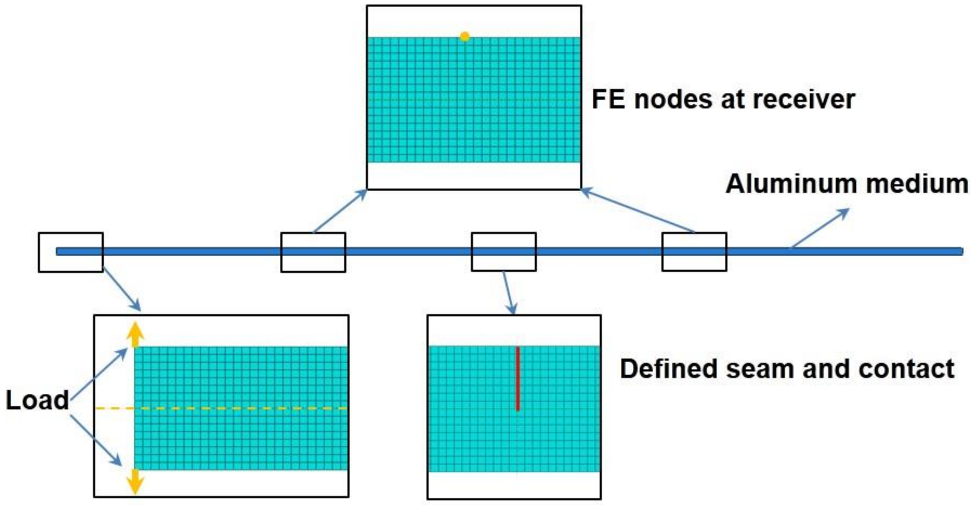
FE nodes at receiver
Aluminum medium
Load
Defined seam and contact

Fig. 8

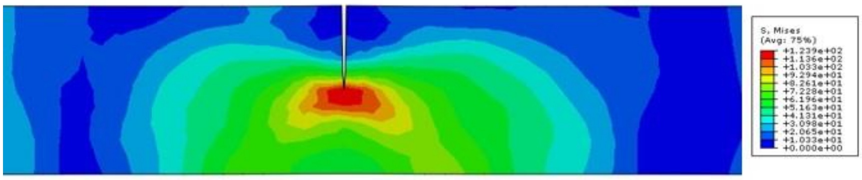
S, Mises
(Avg: 75%)
+1.239e+02
+1.136e+02
+1.033e+02
+9.294e+01
+8.261e+01
+7.228e+01
+6.196e+01
+5.163e+01
+4.131e+01
+3.098e+01
+2.065e+01
+1.033e+01
+0.000e+00

Fig. 9(a)

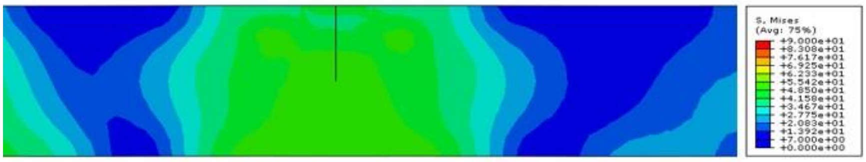
S, Mises
(Avg: 75%)
+9.000e+01
+8.308e+01
+7.617e+01
+6.925e+01
+6.233e+01
+5.542e+01
+4.850e+01
+4.158e+01
+3.467e+01
+2.775e+01
+2.083e+01
+1.392e+01
+7.000e+00
+0.000e+00

Fig. 9(b)

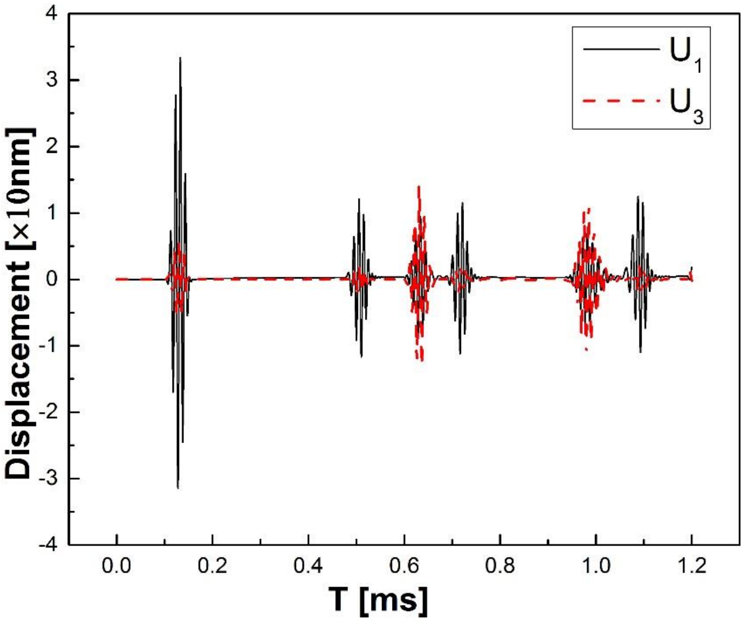

Fig. 10

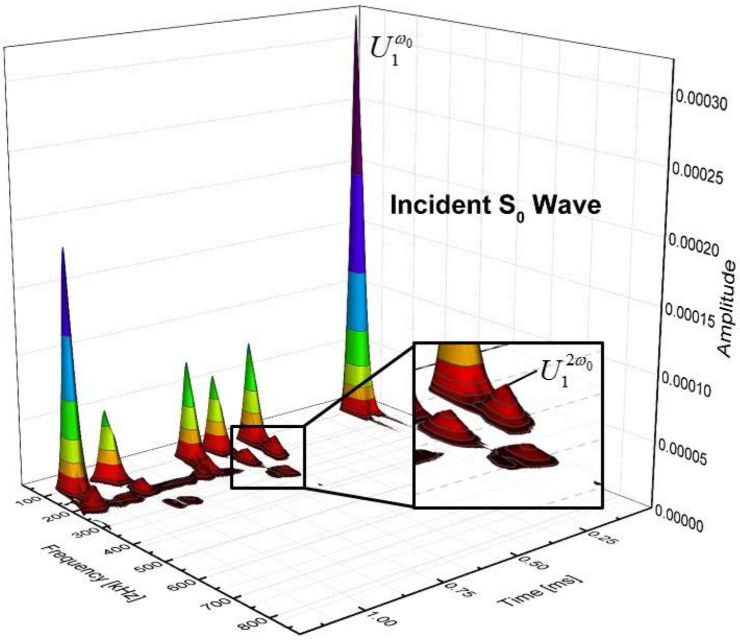

Fig. 11(a)

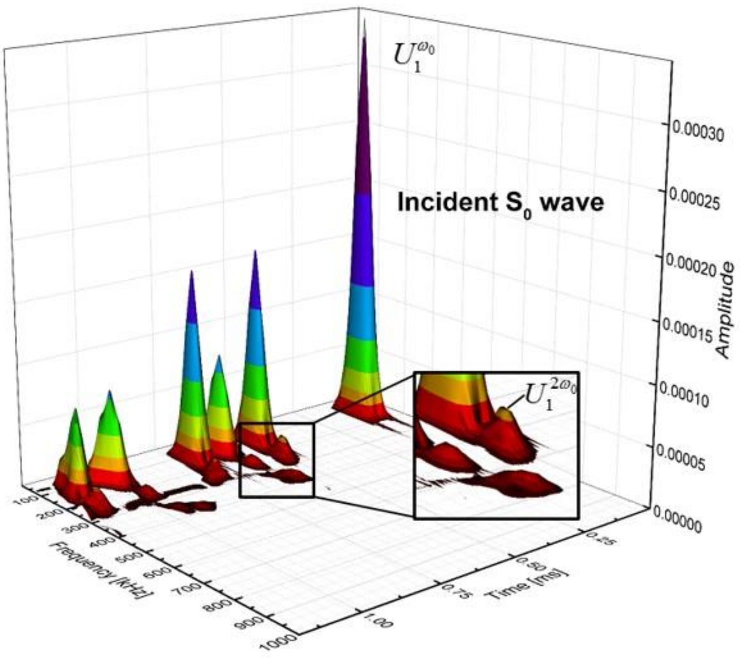

Fig. 11(b)

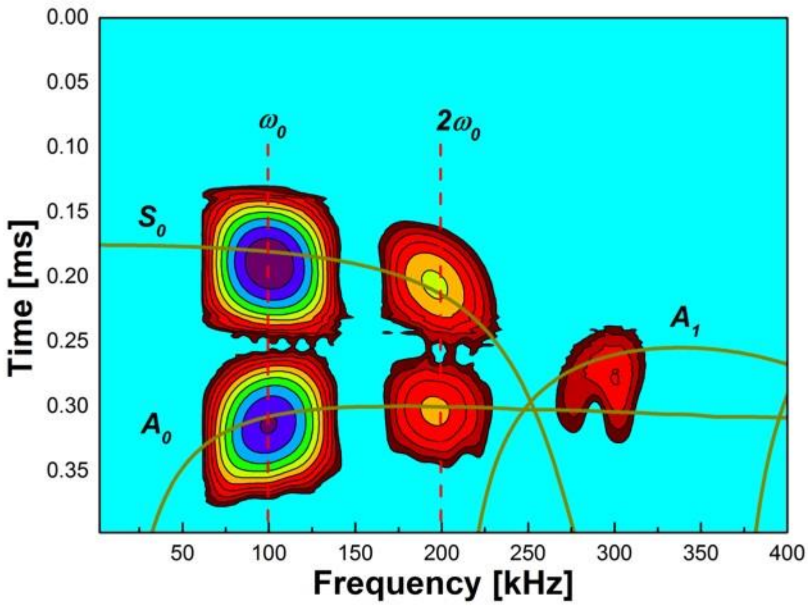

Fig. 12(a)

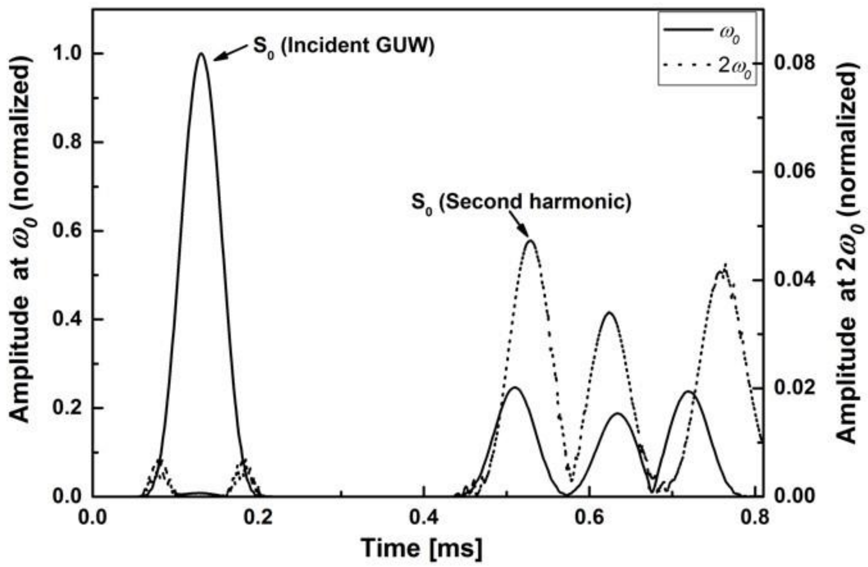

Fig. 12(b)

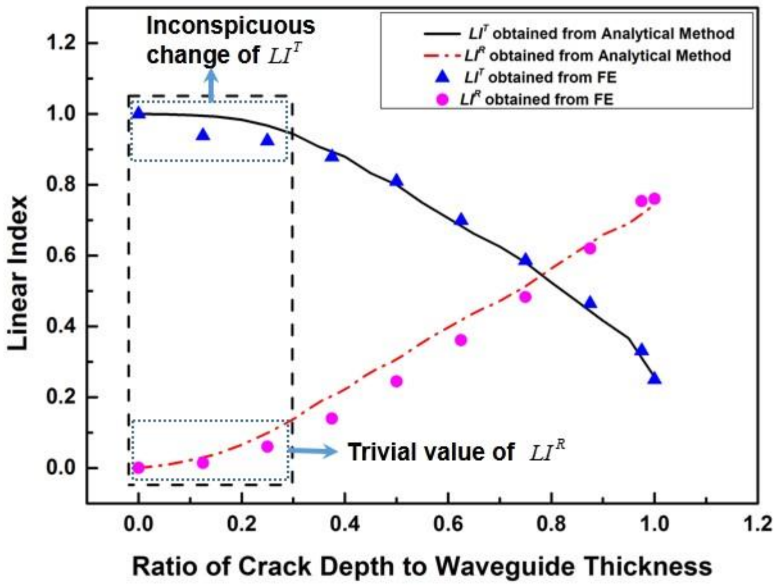

Fig. 13(a)

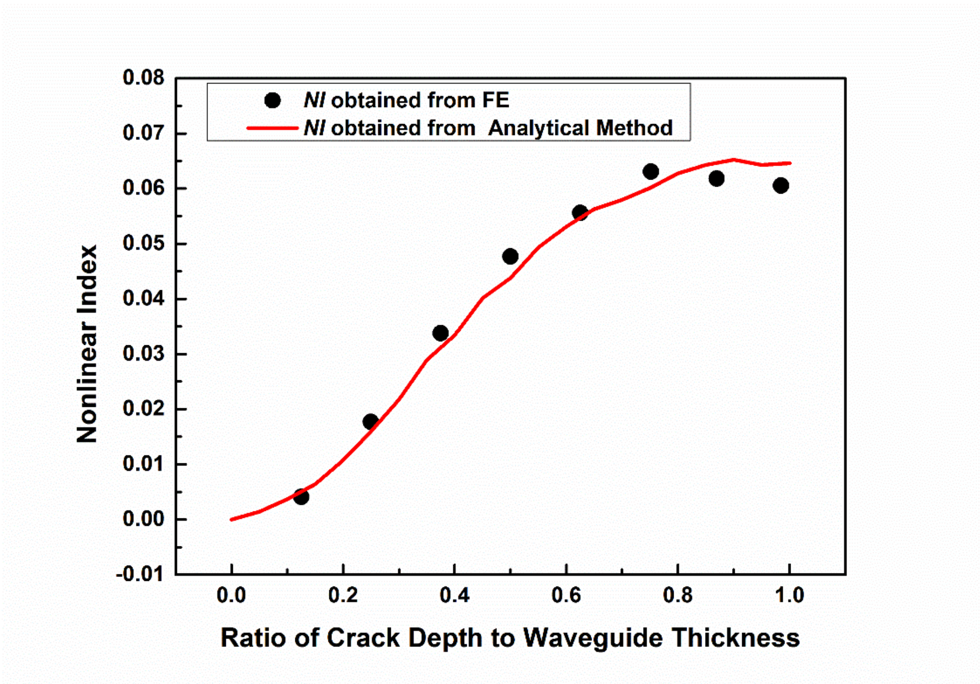

Fig. 13(b)